



Aalborg Universitet

AALBORG UNIVERSITY  
DENMARK

## Second Ripple Current Suppression by Two Bandpass Filters and Current Sharing Method for Energy Storage Converters in DC Microgrid

Yang, Ling; Chen, Yandong; Luo, An; Wu, Wenhua; Huai, Kunshan; Zhou, Xiaoping; Zhou, Leming; Xu, Qianming; Guerrero, Josep M.

*Published in:*

I E E E Journal of Emerging and Selected Topics in Power Electronics

*DOI (link to publication from Publisher):*

[10.1109/JESTPE.2016.2642399](https://doi.org/10.1109/JESTPE.2016.2642399)

*Publication date:*

2017

*Document Version*

Early version, also known as pre-print

[Link to publication from Aalborg University](#)

*Citation for published version (APA):*

Yang, L., Chen, Y., Luo, A., Wu, W., Huai, K., Zhou, X., Zhou, L., Xu, Q., & Guerrero, J. M. (2017). Second Ripple Current Suppression by Two Bandpass Filters and Current Sharing Method for Energy Storage Converters in DC Microgrid. *I E E E Journal of Emerging and Selected Topics in Power Electronics*, 5(3), 1031-1044. <https://doi.org/10.1109/JESTPE.2016.2642399>

### General rights

Copyright and moral rights for the publications made accessible in the public portal are retained by the authors and/or other copyright owners and it is a condition of accessing publications that users recognise and abide by the legal requirements associated with these rights.

- Users may download and print one copy of any publication from the public portal for the purpose of private study or research.
- You may not further distribute the material or use it for any profit-making activity or commercial gain
- You may freely distribute the URL identifying the publication in the public portal -

### Take down policy

If you believe that this document breaches copyright please contact us at [vbn@aub.aau.dk](mailto:vbn@aub.aau.dk) providing details, and we will remove access to the work immediately and investigate your claim.

# Second Ripple Current Suppression by Two Band-Pass Filters and Current Sharing Method for Energy Storage Converters in DC Microgrid

Ling Yang, *Student Member, IEEE*, Yandong Chen, *Member, IEEE*, An Luo, *Senior Member, IEEE*, Wenhua Wu, *Student Member, IEEE*, Kunshan Huai, Xiaoping Zhou, *Student Member, IEEE*, Leming Zhou, Qianming Xu, *Student Member*, and Josep M. Guerrero, *Fellow, IEEE*

**Abstract**—With the increasing of AC loads injected into DC microgrid (MG) through the inverters, the second ripple current (SRC) in the front-end energy storage converter (ESC) and circulating current among the ESCs in DC MG become more and more serious. In this paper, the SRC suppression method by introducing two band-pass filters (BPFs) into the output voltage and inductance current feedback of the ESC is proposed. Compared with the traditional dual-loop control method, the proposed method effectively reduces the SRC and improves the dynamic performance in case of a lower cut-off frequency in the outer voltage loop. Simultaneously, an adaptive droop control method by introducing the fine tuning virtual resistances is adopted to reduce the output voltage deviation of parallel ESCs and improve the output current sharing among the ESCs. Considering the allowed range of the deviation between the output voltage and rated voltage for each ESC, the impacts of the line power loss and circulating current power loss caused by the introduced virtual resistances are analyzed in detail. While the sum of the line power loss and circulating current power loss reaches the minimum value, the appropriate control parameters are obtained. Simulation and experimental results verify the validity of the proposed method.

**Index Terms**—DC microgrid (MG); energy storage converter (ESC); second ripple current (SRC); band-pass filter (BPF); current sharing; virtual resistance

## I. INTRODUCTION

WITH the increasingly serious energy crisis and environmental pollution, renewable energy distributed

Manuscript received September 1, 2016; revised October 9, 2016; accepted December 13, 2016. This work was supported in part by the National Natural Science Foundation of China under Grant 51577056, and in part by the Scientific Research Fund of Hunan Provincial Education Department under Grant YB2016B036.

L. Yang, A. Luo, W. Wu, K. Huai, X. Zhou, L. Zhou, and Q. Xu are with the College of Electrical and Information Engineering, Hunan University, Changsha 410082, China (e-mail: yangling\_1992@163.com; an\_luo@126.com; wenhua\_5@163.com; huai\_kunshan@126.com; zxp2011@hnu.edu.cn; leming\_zhou@126.com; hnuxqm@foxmail.com).

J. M. Guerrero is with the Department of Energy Technology, Aalborg University, 9220 Aalborg East, Denmark (e-mail: joz@et.aau.dk).

Y. Chen is with the College of Electrical and Information Engineering, Hunan University, Changsha 410082, China (corresponding author, phone: +86-731-88823710; fax: +86-731-88823700; e-mail: yandong\_chen@hnu.edu.cn).

generation (DG) has been widely concerned and researched, and MG has also been proposed [1]-[4]. Compared to AC MG, DC MG can shorten the energy conversion chain by reducing the number of DC/AC or AC/DC converters. Meanwhile, they also feature the advantages of higher efficiency, enhanced reliability, lower control complexity, etc. [5]-[6]. Moreover, DC MG can overcome some disadvantages of AC systems, such as transformer inrush current, frequency synchronization, reactive power flow, power quality issues, etc. [7]-[8], and DC MG is developing rapidly.

The low-voltage DC MG is mainly composed of DGs, energy storages (ESs), power converters and AC and DC loads, as shown in Fig. 1. When single-phase inverters with AC loads are injected into DC MG, instantaneous output power of single-phase inverters ripples at double output voltage frequency, which leads to generate the SRC in the front-end ESC. If the peak-to-peak value of the SRC is above 8% of the rated current, it would not only lead to damage to the electrode and electrolyte of the batteries [9], but also reduce the efficiency and lifespan of the batteries [10]. Simultaneously, the SRC also wastes the capacity of the ESCs, influences the lifespan of the power converters [9], and increases the current stress and power loss of the power switching devices [11]. So, it is necessary to suppress the SRC.

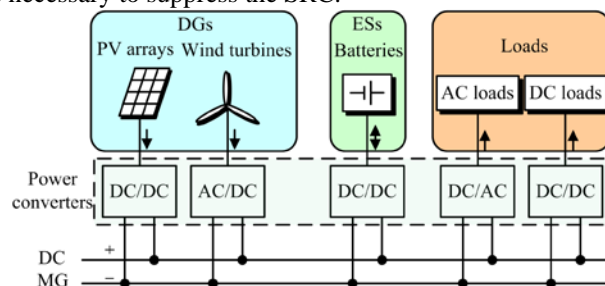


Fig. 1. Generic architecture of low-voltage DC MG.

Considering the impacts of PV converters in MPPT modes, when there is sufficient power and energy reserve within the ESs, the ESs terminals assume DC bus regulation responsibility [12]. The ESCs have three operation modes: buck modes, boost modes and non-working modes. If the load power consumption is below the output power of PV arrays when PV converters are in MPPT modes, the superfluous energy will charge the ESs and the ESCs will work in buck modes. If the load power

consumption is above the output power of PV arrays when PV converters are in MPPT modes, the ESs will be discharged to provide the power deficit and the ESCs will work in boost modes. If the load power consumption is equal to the output power of PV arrays when PV converters are in MPPT modes, the ESs and the ESCs will not work. In these three operation modes, the SRC will penetrate into the PV converters and ESCs. References [13]-[15] have addressed the solutions for the SRC issue in PV converters which realize MPPT of PV arrays, and the SRC in the PV converters is well suppressed. If the existing SRC suppression methods for PV converters which realize MPPT of PV arrays are adopted and the loop gain of the ESCs is relatively high, most of the SRC will penetrate into the ESCs which regulates DC bus voltage. Therefore, when analyzing the SRC alone in the low-voltage standalone DC MG, PV converters in MPPT modes can be omitted [16].

A variety of approaches in reducing the SRC has been proposed in previous publications. A boost DC/DC converter topology with the novel capability has been proposed in [17] to cancel the input current ripple at an arbitrarily preselected duty cycle, which is accomplished without increasing the count of the number of components. In [18], a coupled inductor and an auxiliary inductor are utilized to obtain ripple-free input current and achieve zero-voltage-switching (ZVS) operation of the main and auxiliary switches. A novel high step-up converter has been proposed for a front-end photovoltaic system [19], which not only reduces the current stress through each power switch, but also constrains the input current ripple.

Another approach is to force the SRC in the front-end ESC to flow through DC bus capacitor. In [20], an advanced active control technique has been proposed to incorporate a current control loop in the DC/DC converter for ripple reduction, but the dynamic performance needs to be further improved. The inductance current feedback control method by single BPF has been proposed in [21], which can reduce the closed-loop impedance of the ESC at non-double output voltage frequency and improve the dynamic performance of the system at the load mutation by the BPF, but due to select range limitation of the quality factor, the closed-loop impedance of the ESC at double output voltage frequency in [21] is lower than that in [22]. So, the SRC is less reduced. The capacitance voltage feedback control method by single BPF has been proposed in [22], it effectively reduces the SRC, but there is no single BPF in the inductance current feedback, the closed-loop impedance of the ESC at non-double output voltage frequency in [22] is higher than that in [21], weakening the dynamic performance of the system at the load mutation.

In addition, the circulating current issue will arise if there is a mismatch in the output voltage deviation of parallel ESCs. To solve this problem, a modified droop control method by utilizing the information of no-load circulating current has been proposed in [23] to overcome the effect of error in nominal voltages and reduce the circulating current. References [24]-[25] present a hierarchical control method for the DC/DC converters to suppress the circulating current and improve the system performance. In [26], the droop controller is employed to achieve independent operation and the average voltage and

current controllers are used in each converter to simultaneously enhance the current sharing accuracy and restore DC bus voltage. Distribution voltage control using adaptive droop coefficient in local controller has been proposed to obtain a better voltage regulation in [27]. An adaptive droop scheme is proposed for multiterminal DC grids in [28] to share the load according to the available headroom of converters. An adaptive droop resistance technique can compensate for the adaptive voltage positioning control in a boost DC/DC converter in [29]. But the impact of the output power caused by the line impedance and equivalent output impedance has not been considered in the above methods.

In this paper, the SRC suppression by two BPFs and current sharing method for the ESCs in DC MG is proposed. The paper is organized as follows. The circulating current, SRC are analyzed, and the whole control method for parallel ESCs is proposed in Section II. Section III presents an adaptive droop control method by introducing the fine tuning virtual resistances in series. Section IV shows the SRC suppression method by two BPFs for the ESC. Finally, simulations and experiments are illustrated and discussed in Section V. Some conclusions are given in Section VI.

## II. CIRCULATING CURRENT, SRC ANALYSIS AND PROPOSED CONTROL METHOD FOR PARALLEL ESCS

### A. Analysis of the circulating current among the ESCs

Diagram of parallel ESCs in DC MG with AC loads is shown in Fig. 2. The buck-boost converter named the ESC achieves the bi-directional energy flow between the batteries and DC bus of DC MG. The single-phase full-bridge inverters with LC filters can effectively reduce high-frequency harmonic current. The load is simulated by the DC/AC inverters.

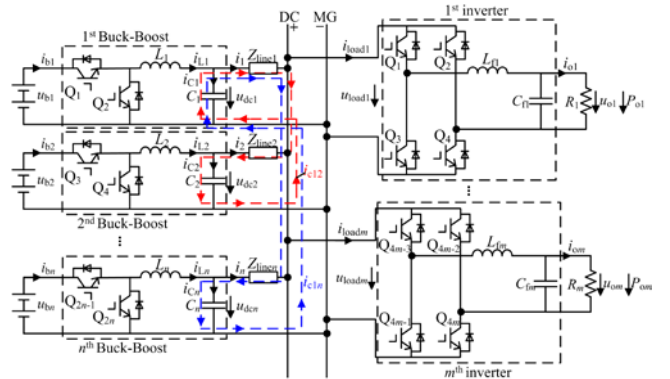


Fig. 2. Diagram of parallel ESCs in DC MG with AC loads.

In Fig. 2,  $u_{bj}$  and  $i_{bj}$  are the output voltage and current of the  $j^{\text{th}}$  ( $j=1, 2, \dots, n$ ) batteries, respectively.  $L_j$  and  $C_j$  are the inductance and capacitance of the  $j^{\text{th}}$  ESC, respectively.  $i_{Lj}$  and  $i_{Cj}$  are separately the currents flowing through  $L_j$  and  $C_j$ .  $u_{dcj}$  and  $i_j$  are the output voltage and current of the  $j^{\text{th}}$  ESC.  $i_{c1j}$  is the circulating current flowing from the 1<sup>st</sup> ESC to the  $j^{\text{th}}$  ESC.  $u_{loadh}$  and  $i_{loadh}$  are the input DC-link voltage and current of the  $h^{\text{th}}$  ( $h=1, 2, \dots, m$ ) inverter, respectively.  $L_{fh}$  and  $C_{fh}$  are the filter inductance and capacitance of the  $h^{\text{th}}$  inverter with AC loads  $R_h$ , respectively.  $u_{oh}$  and  $i_{oh}$  are the output voltage and current of the  $h^{\text{th}}$  inverter, respectively.  $P_{oh}$  is the output active power of AC

loads  $R_h$ . The line impedance is  $Z_{linej} = r_{linej} + jX_{linej}$ . Since the line resistance is much larger than the line reactance in the low-voltage system [2],  $Z_{linej} = r_{linej}$  is assumed and selected in this paper.

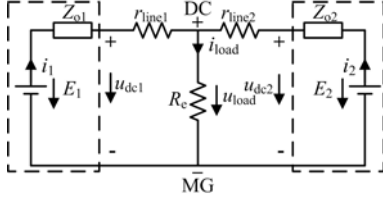


Fig. 3. Simplified diagram of parallel ESCs.

Simplified diagram of parallel ESCs is shown in Fig. 3, where  $E_j$  ( $j = 1, 2$ ) is the output voltage without the load,  $Z_{oj}$  ( $Z_{oj} = r_{oj} + jX_{oj}$ ) is the equivalent output impedance, and  $R_e$  is the equivalent resistance of AC loads connected to DC bus through the inverters.  $i_1$  and  $i_2$  can be expressed as

$$\begin{cases} i_1 = \frac{(r_{line2} + R_e)u_{dc1} - R_e u_{dc2}}{r_{line1}r_{line2} + r_{line1}R_e + r_{line2}R_e} \\ i_2 = \frac{(r_{line1} + R_e)u_{dc2} - R_e u_{dc1}}{r_{line1}r_{line2} + r_{line1}R_e + r_{line2}R_e} \end{cases} \quad (1)$$

The circulating current flowing from the 1<sup>st</sup> ESC to the 2<sup>nd</sup> ESC  $i_{c12}$  can be defined as

$$i_{c12} = -i_{c21} = \frac{u_{dc1} - u_{dc2}}{r_{line1} + r_{line2}} = \frac{i_1 r_{line1} - i_2 r_{line2}}{r_{line1} + r_{line2}} \quad (2)$$

Since  $R_e$  is much larger than the line resistance  $r_{line1}$  and  $r_{line2}$ ,  $r_{line1}r_{line2}$  can be ignored, and  $i_1$  and  $i_2$  can be simplified to

$$\begin{cases} i_1 = \frac{r_{line2}u_{dc1}}{r_{line1}R_e + r_{line2}R_e} + \frac{u_{dc1} - u_{dc2}}{r_{line1} + r_{line2}} \\ i_2 = \frac{r_{line1}u_{dc2}}{r_{line1}R_e + r_{line2}R_e} + \frac{u_{dc2} - u_{dc1}}{r_{line1} + r_{line2}} \end{cases} \quad (3)$$

where  $i'_1$  and  $i'_2$  are the currents flowing from the 1<sup>st</sup> ESC and the 2<sup>nd</sup> ESC to the equivalent load  $R_e$ , respectively.

As a result, the total circulating currents of the  $n^{\text{th}}$  ESCs  $i_{cn}$  can be expressed as

$$\begin{bmatrix} i_{c1} \\ \vdots \\ i_{cn} \end{bmatrix} = \begin{bmatrix} \sum_{m \neq 1}^n \left( \frac{1}{r_{line1} + r_{linem}} \right) & \cdots & \frac{-1}{r_{line1} + r_{linen}} \\ \vdots & \ddots & \vdots \\ \frac{-1}{r_{linen} + r_{line1}} & \cdots & \sum_{m \neq n}^n \left( \frac{1}{r_{linem} + r_{line1}} \right) \end{bmatrix} \begin{bmatrix} u_{dc1} \\ \vdots \\ u_{dcn} \end{bmatrix} \quad (4)$$

where  $i_{cn}$  is the sum of the circulating currents flowing from the  $n^{\text{th}}$  ESC to other ESC.

### B. Mechanism of the SRC for the ESC

The output voltage of the  $h^{\text{th}}$  inverter is supposed to be ideally sinusoidal. For a linear load, the output voltage and current of the  $h^{\text{th}}$  inverter can be expressed as

$$\begin{cases} u_{oh} = U_{oh} \sin(\omega_o t) \\ i_{oh} = I_{oh} \sin(\omega_o t - \varphi) \end{cases} \quad (5)$$

where  $U_{oh}$ ,  $I_{oh}$  and  $\omega_o$  are separately the output voltage amplitude, output current amplitude and angular frequency of the  $h^{\text{th}}$  inverter, and  $\varphi$  is the load impedance angle.

From (5), instantaneous output power of the  $h^{\text{th}}$  inverter can be expressed as

$$p_{oh} = u_{oh} i_{oh} = \frac{1}{2} U_{oh} I_{oh} (\cos \varphi - \cos(2\omega_o t - \varphi)) \quad (6)$$

Supposing the efficiency of the inverter is  $\eta$ . Since the ripple of DC bus voltage  $\Delta u_{dc}$  is very small, DC bus voltage  $u_{dc} = U_{dc}$ . The total instantaneous output power of the inverters can be also expressed as

$$\sum_{h=1}^m p_{oh} = \eta \sum_{h=1}^m p_{inh} = \eta U_{dc} \sum_{j=1}^n i_j \quad (7)$$

where  $p_{inh}$  is instantaneous input power of the  $h^{\text{th}}$  inverter. So, the output current of the  $j^{\text{th}}$  ESC can be expressed as

$$\begin{aligned} i_j &= \lambda_j \frac{1}{\eta} \sum_{h=1}^m \left[ \frac{1}{2U_{dc}} U_{oh} I_{oh} (\cos \varphi - \cos(2\omega_o t - \varphi)) \right] \\ &= I_{dcj} + i_{2ndj} \end{aligned} \quad (8)$$

where  $\lambda_j$  is the proportion coefficient of instantaneous output power of the  $j^{\text{th}}$  ESC,  $\sum_{j=1}^n \lambda_j = 1$ .

According to (8), the output current  $i_j$  is mainly composed of two components. One is DC component  $I_{dcj}$ , and the other is the SRC  $i_{2ndj}$ .  $I_{dcj}$  and  $i_{2ndj}$  can be expressed as

$$\begin{cases} I_{dcj} = \lambda_j \frac{1}{2U_{dc}\eta} \sum_{h=1}^m (U_{oh} I_{oh} \cos \varphi) \\ i_{2ndj} = \lambda_j \frac{1}{2U_{dc}\eta} \sum_{h=1}^m (U_{oh} I_{oh} \cos(2\omega_o t - \varphi)) \end{cases} \quad (9)$$

Equivalent circuit diagram of the single ESC is shown in Fig. 4. It is obvious that  $i_{2ndj}$  will flow into the inductance  $L_j$  and capacitance  $C_j$  of the  $j^{\text{th}}$  ESC. So, there will be the SRC in  $i_{Lj}$  and  $i_{Cj}$ . The SRC in  $i_{Lj}$  increases the current stress and power loss of the power switching devices. Therefore, it is necessary to suppress the SRC in the inductance current.

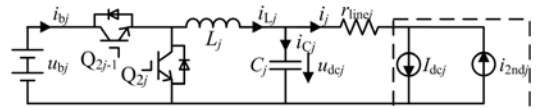


Fig. 4. Equivalent circuit diagram of the single ESC.

### C. Proposed control method for parallel ESCs

As shown in Fig. 5, the SRC suppression method by introducing two BPFs into the output voltage and inductance current feedback of the ESC is proposed, and an adaptive droop control method by introducing the fine tuning virtual resistances is adopted to sharing currents among the ESCs.  $R_{droopj}$  and  $R'_{droopj}$  are separately the non-fine-tuning and fine-tuning virtual resistances of the  $j^{\text{th}}$  ESC.  $u_{dc\_ref}^*$  is the output voltage reference of the ESC when the fine tuning virtual resistances are introduced into the output voltage and inductance current feedback of the ESC.  $i_{Lj}^*$  is the inductance current reference of the  $j^{\text{th}}$  ESC.  $G_i(s)$  is the transfer function of

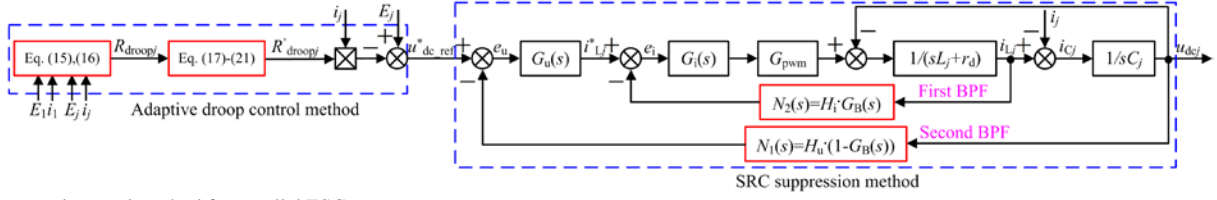


Fig. 5. Proposed control method for parallel ESCs.

PI controller in the outer voltage loop.  $G_i(s)$  is the transfer function of P controller in the inner current loop.  $G_{pwm}$  is the gain of the ESC.  $G_B(s)$  is the transfer function of the BPF.  $N_1(s) = H_u(1 - G_B(s))$  and  $N_2(s) = H_i G_B(s)$  are separately the feedback coefficients of the capacitance voltage and inductance current.  $H_u$  and  $H_i$  are separately the sensor coefficients of the capacitance voltage and inductance current.  $r_d$  is the equivalent resistance connected to the inductance in series.

### III. THE ADAPTIVE DROOP CONTROL METHOD FOR PARALLEL ESCS

To reduce the output voltage deviation of parallel ESCs and improve the output current sharing among the ESCs, an adaptive droop control method by introducing the fine tuning virtual resistances is adopted as shown in Fig. 5. Simplified diagram of parallel ESCs with the virtual resistances is shown in Fig. 6. The droop control with the virtual resistances can be expressed as

$$\begin{cases} u_{dc1\_ref} = E_1 - i_1 Z_{o1} - i_1 R_{droop1} \\ u_{dc2\_ref} = E_2 - i_2 Z_{o2} - i_2 R_{droop2} \end{cases} \quad (10)$$

where  $u_{dc1\_ref}$  and  $u_{dc2\_ref}$  are separately the output voltage references when the virtual resistances are introduced into the 1<sup>st</sup> ESC and the 2<sup>nd</sup> ESC.

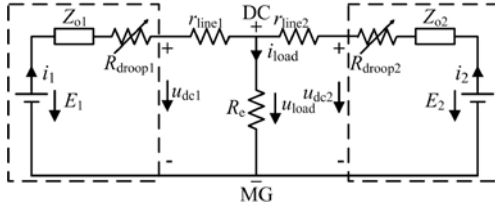


Fig. 6. Simplified diagram of parallel ESCs with the virtual resistances.

Since the equivalent output reactance can be ignored, the equivalent impedances are expressed as  $Z_{o1} = r_{o1}$  and  $Z_{o2} = r_{o2}$  under the DC component. The relationship between the virtual resistances can be expressed as

$$R_{droop1}/R_{droop2} = R_1/R_2 \quad (11)$$

where  $R_1 = r_{o1} + r_{line1}$ , and  $R_2 = r_{o2} + r_{line2}$ .

Considering the line resistances, the line power loss of the ESC can be expressed as

$$P_{line} = i_1^2 r_{line1} + i_2^2 r_{line2} \quad (12)$$

The output currents of the 1<sup>st</sup> ESC  $i_1$  and the 2<sup>nd</sup> ESC  $i_2$  can be expressed as

$$\begin{cases} i_1 = \frac{(C + R_e)AE_2 - R_e E_2}{X} \\ i_2 = \frac{(BC + R_e)E_2 - R_e AE_2}{X} \end{cases} \quad (13)$$

where  $A = E_1/E_2$ ,  $B = R_1/R_2$ ,  $C = R_2 + R_{droop2}$ , and  $X = BC^2 + (1 + B)CR_e$ .

Therefore, the circulating current  $i_{c12}$  can be expressed as

$$i_{c12} = -i_{c21} = E_2 \cdot \frac{Dr_{line1} - Fr_{line2}}{X(r_{line1} + r_{line2})} \quad (14)$$

where  $D = AC + (A - 1)R_e$ , and  $F = BC + (1 - A)R_e$ .

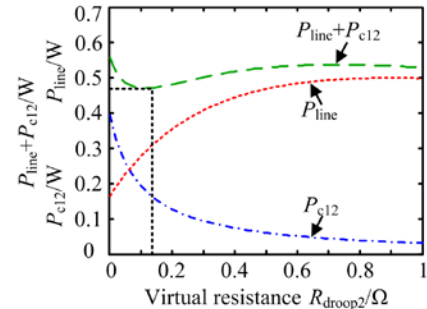
The circulating current power loss can be expressed as

$$P_{c12} = E_2^2 \cdot \frac{D^2 r_{line1}^2 - 2DFr_{line1}r_{line2} + F^2 r_{line2}^2}{X^2 (r_{line1} + r_{line2})} \quad (15)$$

Using (12) and (13), the line power loss can be expressed as

$$P_{line} = E_2^2 \cdot \frac{D^2 r_{line1} + F^2 r_{line2}}{[BC^2 + (1 + B)CR_e]^2} \quad (16)$$

From Fig. 5, the input variables  $E_j$  ( $j = 1, 2$ ) and  $i_j$  can obtain the line power loss  $P_{line}$  and circulating current power loss  $P_{c12}$  by using (15) and (16). The relationship curves between the line power loss  $P_{line}$ , the circulating current power loss  $P_{c12}$ ,  $P_{line} + P_{c12}$  and  $R_{droop2}$  are shown in Fig. 7, where  $P_{line}$  increases and  $P_{c12}$  decreases continuously with increase in  $R_{droop2}$ . Considering the allowed range of the deviation between the output voltage and rated voltage for each ESC, while the sum of  $P_{line}$  and  $P_{c12}$  reaches the minimum value, the appropriate  $R_{droop2}$  is obtained.


 Fig. 7. Relationship curves between the line power loss  $P_{line}$ , the circulating current power loss  $P_{c12}$ ,  $P_{line} + P_{c12}$  and  $R_{droop2}$ .

The output voltages of parallel ESCs may have a certain deviation when the virtual resistances are introduced into parallel ESCs. So, the virtual resistances have to be fine tuned to make the output voltages of parallel ESCs equivalent. Droop characteristics of the fine tuning virtual resistances are shown in Fig. 8, where  $m_1$  and  $m_2$  are the droop control curves of the 1<sup>st</sup> ESC and the 2<sup>nd</sup> ESC with the non-fine-tuning virtual resistances, respectively,  $m_3$  and  $m_4$  are the droop control curves of the 1<sup>st</sup> ESC and the 2<sup>nd</sup> ESC with the fine-tuning virtual resistances, respectively, and  $\Delta u_1$  and  $\Delta u_2$  are the variations of the voltages  $u_{dc1}$  and  $u_{dc2}$  of the 1<sup>st</sup> ESC and the 2<sup>nd</sup> ESC from introducing the non-fine-tuning virtual resistances to fine-tuning virtual resistances, respectively.

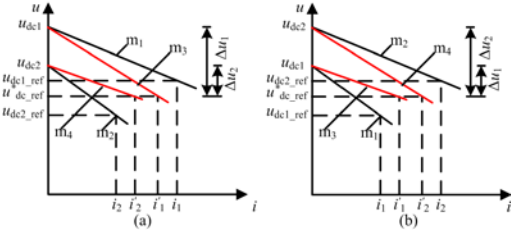


Fig. 8. Droop characteristics of the fine tuning virtual resistances. (a)  $(u_{dc1} - u_{dc2}) > 0$ . (b)  $(u_{dc1} - u_{dc2}) < 0$ .

From Fig. 8(a), if  $(u_{dc1} - u_{dc2}) > 0$ , the fine tuning virtual resistances  $R'_{droop1}$  and  $R'_{droop2}$  can be expressed as

$$\begin{cases} R'_{droop1} = R_{droop1} + k_1 i_{load} \\ R'_{droop2} = R_{droop2} - k_2 i_{load} \end{cases} \quad (17)$$

where  $k_1$  and  $k_2$  are the droop correction parameters.  $k_2 > k_1$  is selected in order to make the drop-out values of the output voltages of parallel ESCs within a certain range.

Using (10) and (17), if  $(u_{dc1} - u_{dc2}) > 0$ , the droop correction parameters  $k_1$  and  $k_2$  can be expressed as

$$\begin{cases} k_1 = (X \varepsilon_u - DE_2 R_{droop1}) / DE_2 i_{load} \\ k_2 = (FE_2 R_{droop2} - X \varepsilon_u) / FE_2 i_{load} \end{cases} \quad (18)$$

where  $\varepsilon_u$  is the half of the allowed maximum output voltage deviation of parallel ESCs.

From Fig. 8(b), if  $(u_{dc1} - u_{dc2}) < 0$ , the fine tuning virtual resistances  $R'_{droop1}$  and  $R'_{droop2}$  can be expressed as

$$\begin{cases} R'_{droop1} = R_{droop1} - k_2 i_{load} \\ R'_{droop2} = R_{droop2} + k_1 i_{load} \end{cases} \quad (19)$$

Using (10) and (19), if  $(u_{dc1} - u_{dc2}) < 0$ , the droop correction parameters  $k_1$  and  $k_2$  can be expressed as

$$\begin{cases} k_1 = (X \varepsilon_u - FE_2 R_{droop2}) / FE_2 i_{load} \\ k_2 = (DE_2 R_{droop1} - X \varepsilon_u) / DE_2 i_{load} \end{cases} \quad (20)$$

While  $(u_{dc1} - u_{dc2}) = 0$ , the fine tuning virtual resistances  $R'_{droop1}$  and  $R'_{droop2}$  can be expressed as

$$\begin{cases} R'_{droop1} = R_{droop1} \\ R'_{droop2} = R_{droop2} \end{cases} \quad (21)$$

From Fig. 5, the virtual resistances  $R_{droopj}$  can change into the fine tuning virtual resistances  $R'_{droopj}$  by using (17) to (21). Meanwhile, the output voltages of parallel ESCs are equivalent when the fine tuning virtual resistances are introduced into parallel ESCs. So, the adaptive droop control method eliminates the circulating current and improves the output current sharing between parallel ESCs.

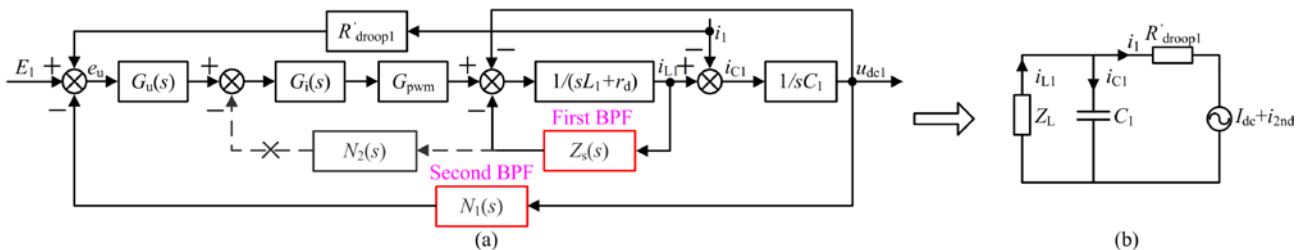


Fig. 9. The equivalent transformation diagram of the proposed SRC suppression method. (a) Control diagram of the equivalent transformation. (b) Construction circuit of the SRC

#### IV. THE SRC SUPPRESSION METHOD BY TWO BPFs FOR THE ESC

##### A. The SRC suppression method by two BPFs and its dynamic performance analysis

The equivalent transformation diagram of the SRC suppression method is shown in Fig. 9. The feedback of the inductance current  $i_{L1}$  is moved back to the output of PWM from the input of P controller in the inner current loop. The virtual impedance  $Z_s(s)$  can be expressed

$$Z_s(s) = N_2(s)G_i(s)G_{pwm} \quad (22)$$

Different feedback coefficients of the SRC suppression method are given out in Tab. I. The impacts of the SRC suppression and dynamic performance caused by the feedback coefficients are analyzed, and the appropriate control parameters are selected while the SRC suppression and dynamic performance are the best.

TABLE I  
DIFFERENT FEEDBACK COEFFICIENTS OF THE SRC SUPPRESSION METHOD

Feedback coefficients	$N_1(s)$	$N_2(s)$
Case I	$H_u$	$H_i$
Case II	$H_u$	$H_i G_B(s)$
Case III	$H_u(1 - G_B(s))$	$H_i$
Case IV	$H_u(1 - G_B(s))$	$H_i G_B(s)$

From Fig. 9(b), the SRC in the inductance current  $i_{L1}$  depends on the capacitance  $C_1$  connected to the closed-loop impedance  $Z_L$  in parallel. Assumed that the capacitance  $C_1$  is constant, the closed-loop impedance  $Z_L$  increases in order to decrease the SRC in the inductance current  $i_{L1}$ . The closed-loop impedance  $Z_L$  can be expressed as

$$Z_L = \frac{sL_1 + r_d + Z_s(s)}{1 + G_u(s)G_i(s)G_{pwm}N_1(s)} \quad (23)$$

The outer voltage loop gain can be expressed as

$$T_u(s) = \frac{G_u(s)G_i(s)G_{pwm}N_1(s)}{sC_1(sL_1 + r_d + Z_s(s)) + 1} \quad (24)$$

The transfer function of the closed-loop of the system can be expressed as

$$\Phi(s) = G_u(s)G_i(s)G_{pwm} / M \quad (25)$$

where  $M = sC_1(sL_1 + r_d + Z_s(s)) + G_u(s)G_i(s)G_{pwm}N_1(s) + 1$ .

Bode diagrams of the closed-loop impedances are shown in Fig. 10. The closed-loop impedance presents high impedance at the whole output voltage frequency in the case I. So, the SRC suppression and dynamic performance of the system at the load mutation need to be improved. Compared to the cases I and II, the amplitude of the closed-loop impedance reaches the

maximum value at double output voltage frequency in the cases III and IV, which effectively reduce the SRC.

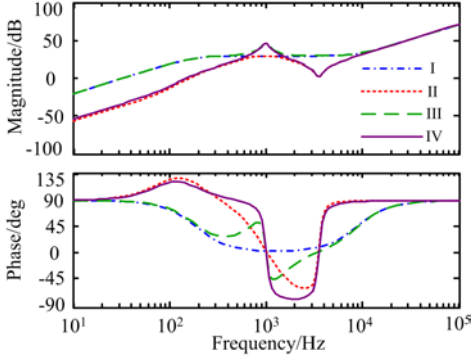


Fig. 10. Bode diagrams of the closed-loop impedances.

Magnitude-frequency curves of the outer voltage loop gains are shown in Fig. 11, where  $f_o$  is the frequency of the output voltage for the  $h^{\text{th}}$  inverter. The instantaneous output power of the  $h^{\text{th}}$  inverter ripples at double output voltage frequency, which leads to generate the SRC with the same frequency in the ESC. Compared to the cases I and III, the cut-off frequencies in the outer voltages loop are increased in the cases II and IV, which improve the dynamic performance in case of a very low cut-off frequency in the outer voltage loop in the case I.

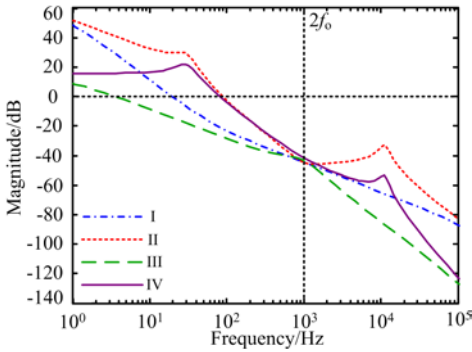


Fig. 11. Magnitude-frequency curves of the outer voltage loop gains.

Unit step dynamic responses of the ESC are shown in Fig. 12. Compared to the cases I and III, the regulation time and overshoot are the minimum value in the cases II and IV, which improve the dynamic performance of the system at the load mutation. So, the SRC suppression method by two BPFs not only effectively reduces the SRC, but also improves the dynamic performance of the system at the load mutation.

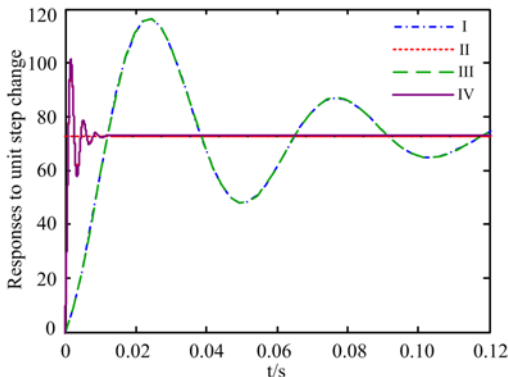


Fig. 12. Unit step dynamic responses of the ESC.

### B. The control parameters selection and stability analysis

The transfer function of the BPF  $G_B(s)$  can be expressed as

$$G_B(s) = \frac{2\omega_o s/Q}{s^2 + 2\omega_o s/Q + (2\omega_o)^2} \quad (26)$$

where  $Q$  is the quality factor of the BPF.

Bode diagrams of the BPF with  $Q = 0.25, 1, 2$  are shown in Fig. 13. The function of the BPF is that the signals are allowed to pass within a certain range of the transmission band. Meanwhile, the signals that are lower than the minimal limit frequency and higher than the maximal limit frequency are attenuated and inhibited. The larger value of  $Q$  is, the better wave-passed characteristic is, but the smaller range of the frequency is. System responses to unit step change with  $Q = 0.25, 1, 2$  are shown in Fig. 14. The regulation time and overshoot increase when  $Q$  enlarges, which can influence the dynamic performance of the ESC at the load mutation. So,  $Q = 1$  is selected when the wave-passed characteristic and dynamic performance are considered.

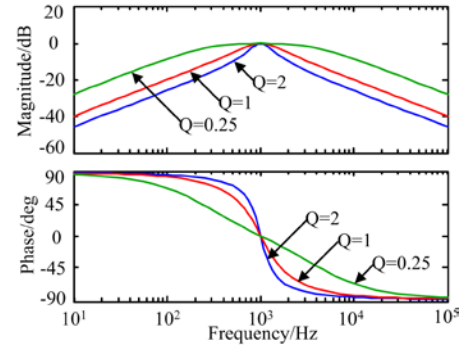


Fig. 13. Bode diagrams of the BPF with  $Q = 0.25, 1, 2$ .

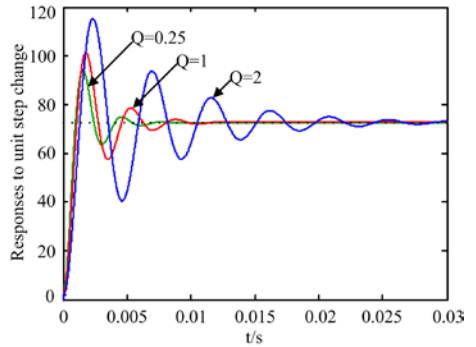


Fig. 14. System responses to unit step change with  $Q = 0.25, 1, 2$ .

Using (25), the characteristic root equation of the closed-loop transfer function of the system can be expressed as

$$T_1 s^5 + T_2 s^4 + T_3 s^3 + T_4 s^2 + T_5 s^1 + T_6 s^0 = 0 \quad (27)$$

where

$$\begin{cases} T_1 = QL_1 C_1 \\ T_2 = 2\omega_o L_1 C_1 + QC_1 r_d \\ T_3 = (2\omega_o)^2 QL_1 C_1 + 2\omega_o C_1 (r_d + r_c) + Q(k_p G_{pwm} H_u + 1) \\ T_4 = (2\omega_o)^2 QC_1 r_d + Qk_i G_{pwm} H_u + 2\omega_o \\ T_5 = (2\omega_o)^2 Q(k_p G_{pwm} H_u + 1) \\ T_6 = (2\omega_o)^2 Qk_i G_{pwm} H_u \end{cases}$$

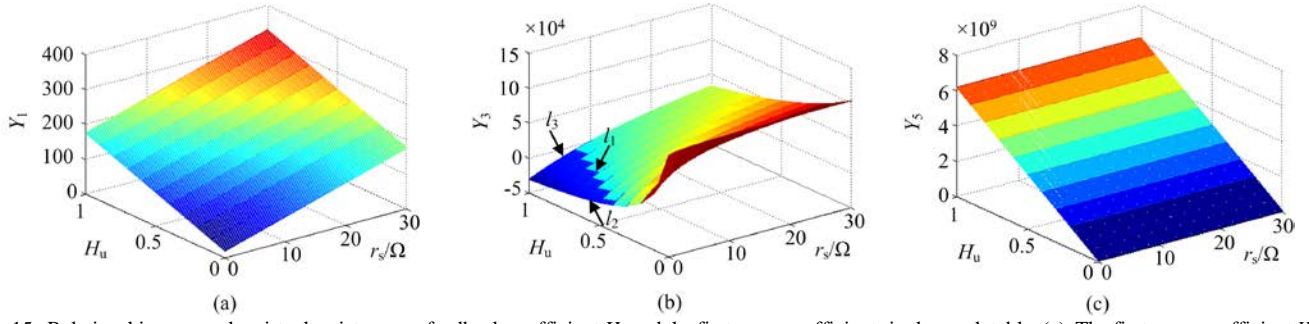


Fig. 15. Relationship among the virtual resistance  $r_s$ , feedback coefficient  $H_u$  and the first array coefficients in the routh table. (a) The first array coefficient  $Y_1$ . (b) The first array coefficient  $Y_3$ . (c) The first array coefficient  $Y_5$ .

$k_p$  and  $k_i$  are the parameters of PI controller in the outer voltage loop,  $r_s$  is the virtual impedance  $Z_s(s)$  when the feedbacks are not added into the BPF, and  $r_s = H_i G_i G_{pwm}$ .

TABLE II

ROUTH TABLE OF THE CLOSED-LOOP SYSTEM				
Rank	Routh array			
$s^5$	$T_1$		$T_3$	$T_5$
$s^4$	$T_2$		$T_4$	$T_6$
$s^3$	$Y_1 = (T_2 T_3 - T_1 T_4) / T_2$	$Y_2 = (T_2 T_5 - T_1 T_6) / T_2$		0
$s^2$	$Y_3 = (Y_1 T_4 - T_2 Y_2) / Y_1$	$Y_4 = T_6$		0
$s^1$	$Y_5 = (Y_3 Y_2 - Y_1 Y_4) / Y_3$		0	0
$s^0$	$Y_6 = T_6$		0	0

Routh table of the closed-loop system is shown in Tab. II. The first array coefficients of the routh table must be positive in order to meet the steady condition of the closed-loop system. In other words, the characteristic roots are all in the left-half plane of  $s$ . Relationship among the virtual resistance  $r_s$ , feedback coefficient  $H_u$  and the first array coefficients in the routh table are shown in Fig. 15. From Fig. 15(a),  $Y_1$  is always above zero with changes in the virtual resistance  $r_s$  and feedback coefficient  $H_u$ . From Fig. 15(b), when the feedback coefficient  $H_u$  is constant,  $Y_3$  increases continuously with increase in the virtual resistance  $r_s$ . When the virtual resistance  $r_s$  is constant,  $Y_3$  decreases continuously with increase in the feedback coefficient  $H_u$ . The part surrounded by the curves  $l_1$ ,  $l_2$  and  $l_3$  indicates  $Y_3$  is below zero. From Fig. 15(c),  $Y_5$  is always above zero with changes in the virtual resistance  $r_s$  and feedback coefficient  $H_u$ . Therefore, when the virtual resistance  $r_s$  and feedback coefficient  $H_u$  are not in the part surrounded by the curves  $l_1$ ,  $l_2$  and  $l_3$ , the closed-loop system is steady.

### C. Impact of the equivalent output resistance of the proposed control method

Under the DC component and the SRC, the equivalent output impedance of each ESC is designed to the larger resistance in order to effectively eliminate the effect of the different line resistances, suppress the circulating current and realize the output current sharing among the ESCs.

Bode diagrams of the equivalent output impedances under the different control methods are shown in Fig. 16. The control method without the virtual resistance and SRC suppression is defined as “the control method A”. The control method with the virtual resistances but not introducing the SRC suppression is defined as “the control method B”. The control method with the adaptive droop control method but not introducing the SRC suppression is defined as “the control method C”. The proposed

control method is defined as “the control method D”.

Using the control method A, the equivalent output impedance  $Z_{o1}$  can be expressed as

$$Z_{o1} = \frac{L_1 s^2 + (r_d + r_s) s}{A_3(s) s^3 + A_2(s) s^2 + A_1(s) s + A_0(s)} \quad (28)$$

where

$$\begin{cases} A_3(s) = L_1 C_1 \\ A_2(s) = C_1 (r_d + r_s) \\ A_1(s) = 1 + k_p G_i G_{pwm} H_u \\ A_0(s) = k_i G_i G_{pwm} H_u \end{cases}$$

The control method B and C are similar. So, taking the control method C as the study object, the equivalent output impedance  $Z'_{o1}$  can be expressed as

$$Z'_{o1} = R'_{droop1} + Z_{o1} \quad (29)$$

Using the proposed control method, the equivalent output impedance  $Z''_{o1}$  can be expressed

$$Z''_{o1} = (B_5(s) s^5 + B_4(s) s^4 + B_3(s) s^3 + B_2(s) s^2 + B_1(s) s^1 + B_0(s)) / (D_5(s) s^5 + D_4(s) s^4 + D_3(s) s^3 + D_2(s) s^2 + D_1(s) s^1 + D_0(s)) \quad (30)$$

where

$$\begin{cases} B_5(s) = R'_{droop1} Q L_1 C_1 \\ B_4(s) = Q L_1 + R'_{droop1} C_1 (2\omega_o L_1 + Q r_d) \\ B_3(s) = 2\omega_o L_1 + Q r_d + R'_{droop1} \{ Q + Q k_p G_i G_{pwm} H_u + C_1 [(2\omega_o)^2 Q L_1 + 2\omega_o (r_d + r_s)] \} \\ B_2(s) = (2\omega_o)^2 Q L_1 + 2\omega_o (r_d + r_s) + R'_{droop1} [2\omega_o + Q k_i G_i G_{pwm} H_u + (2\omega_o)^2 Q r_d C_1] \\ B_1(s) = (2\omega_o)^2 Q r_d + R'_{droop1} (2\omega_o)^2 Q (1 + k_p G_i G_{pwm} H_u) \\ B_0(s) = R'_{droop1} (2\omega_o)^2 Q k_i G_i G_{pwm} H_u \\ D_5(s) = Q L_1 C_1 \\ D_4(s) = C_1 (2\omega_o L_1 + Q r_d) \\ D_3(s) = Q (1 + k_p G_i G_{pwm} H_u) + C_1 [(2\omega_o)^2 Q L_1 + 2\omega_o (r_d + r_s)] \\ D_2(s) = 2\omega_o + Q k_i G_i G_{pwm} H_u + (2\omega_o)^2 Q r_d C_1 \\ D_1(s) = (2\omega_o)^2 Q (1 + k_p G_i G_{pwm} H_u) \\ D_0(s) = (2\omega_o)^2 Q k_i G_i G_{pwm} H_u \end{cases}$$

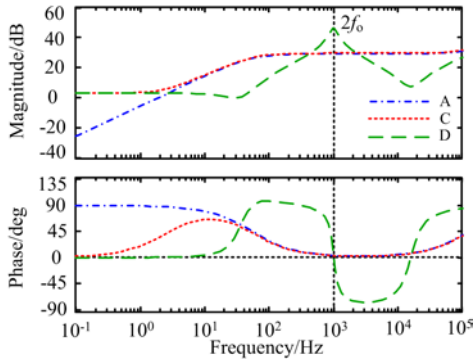


Fig. 16. Bode diagrams of the equivalent output impedances under the different control methods.

From Fig. 16, compared to the control method A, the equivalent output impedance  $Z'_{o1}$  is the larger resistance in the low frequency range in the control method C, which decreases the effect of the different line resistances, but the influence of the SRC is not considered. Compared to the control method C, the proposed control method not only has the advantages of the control method C, but also makes the equivalent output impedance  $Z'_{o1}$  be resistive and the larger amplitude at double output voltage frequency, which is in favor of the circulating current suppression among the ESCs, realizes the output current sharing and effectively reduces the SRC.

V. SIMULATION AND EXPERIMENT

The In order to verify the validity of the proposed control method, the simulation model of parallel ESCs in the low-voltage DC MG is built by using PSIM 9.0 based on the Fig. 2. System parameters are shown in Tab. III.

TABLE III  
SYSTEM PARAMETERS

Parameters	Value	Parameters	Value
$U_{dc}/V$	41	$R_{droop1}/m\Omega$	140
$U_o/V$	22	$R_{droop2}/m\Omega$	168
$U_m/V$	2	$k_p$	1.5
$L_1/mH$	1.2	$k_i$	0.01
$L_2/mH$	1.2	$k$	0.95
$C_1/\mu F$	8000	$H_0$	0.137
$C_2/\mu F$	8000	$H_1$	0.1
$L_f/mH$	5	$k_1$	0.001
$C_f/\mu F$	3.3	$k_2$	0.02
$r_q/\Omega$	3	$f_s/kHz$	12.8
$r_{line1}/m\Omega$	100	$f_o/Hz$	500
$r_{line2}/m\Omega$	120	$f_i/kHz$	1.24

The single group of single-phase AC loads is injected into DC MG, and its active power is approximately equal to 200W. The simulation results of the output voltage  $u_{dcj}$ , output current  $i_j$ , circulating current  $i_{c1j}$ , output power  $P_j$  and inductance current  $i_{Lj}$  under different control methods with single group AC loads are shown in Fig. 17. From Fig. 17(a), during time

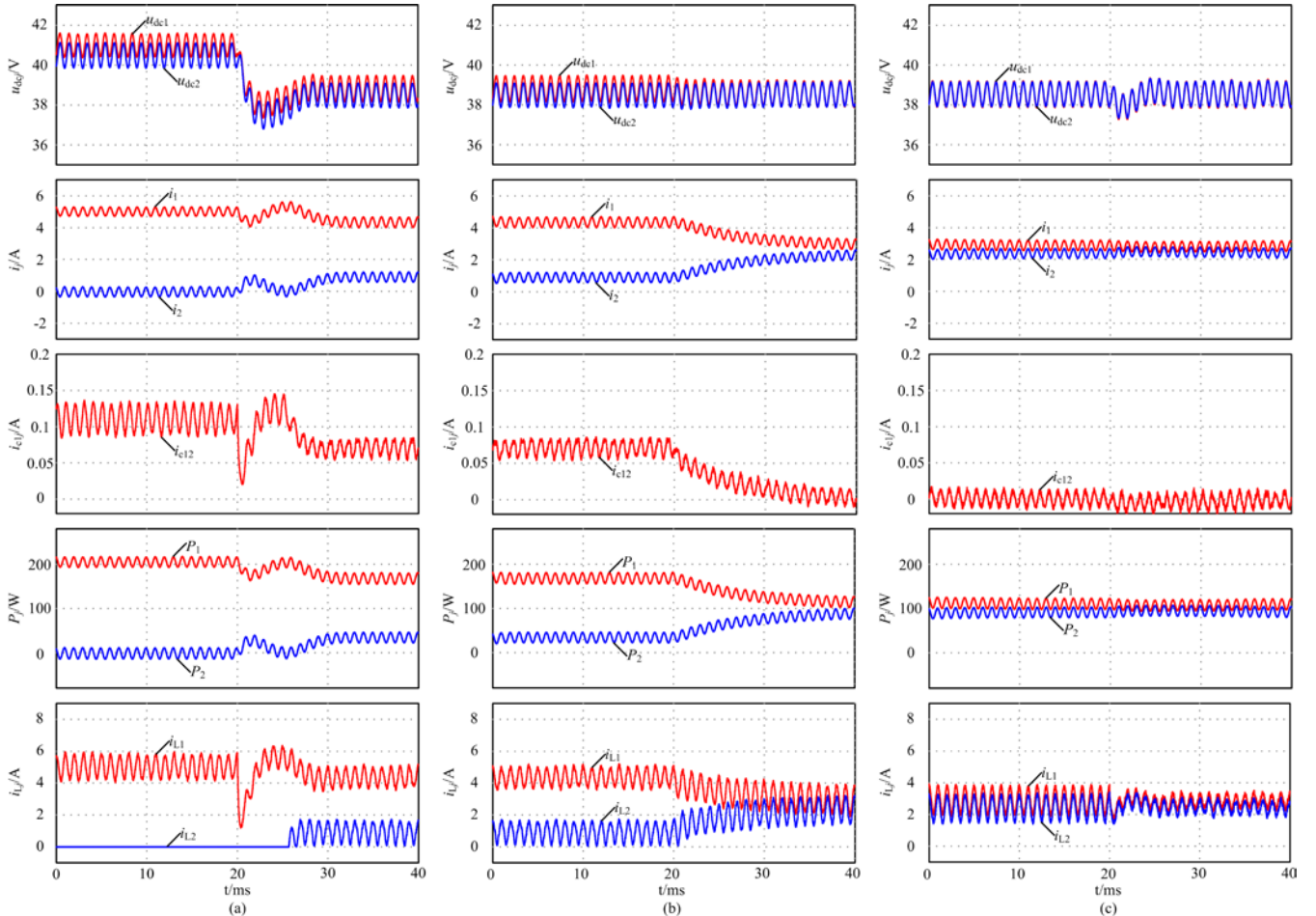


Fig. 17. Simulation results of the output voltage  $u_{dcj}$ , output current  $i_j$ , circulating current  $i_{c1j}$ , output power  $P_j$  and inductance current  $i_{Lj}$  under different control methods with single group AC loads. (a) the control method A and B. (b) the control method B and C. (c) the control method C and D.

0-20 ms, the control method A is used to simulate for each ESC. During time 20-40 ms, the control method B is used to simulate for each ESC. Initially, up to 20 ms, the output voltage of the 2<sup>nd</sup> ESC is decreased by 1% of its nominal value 41V. At time 30 ms, the deviation between the output voltage and the rated voltage for each ESC is 5% within the acceptable range, but the output voltages of parallel ESCs may have a certain deviation. Compared to the control method A, the control method B reduces the output voltage deviation of parallel ESCs and suppresses the circulating current.

From Fig. 17(b), during time 0-20 ms, the control method B is used to simulate for each ESC. During time 20-40 ms, the control method C is used to simulate for each ESC. Initially, up to 20 ms, the deviation between the output voltage and the rated voltage for each ESC is 5% within the acceptable range, but the output voltages of parallel ESCs may have a certain deviation. At time 30 ms, the output voltage of the 2<sup>nd</sup> ESC is equal to the output voltage of the 1<sup>st</sup> ESC. Compared to the control method B, the control method C makes the output voltages of parallel ESCs equivalent, eliminates the circulating current and improves the output current sharing between parallel ESCs.

From Fig. 17(c), during time 0-20 ms, the control method C is used to simulate for each ESC. During time 20-40 ms, the control method D is used to simulate for each ESC. Initially, up to 20 ms, the peak-to-peak of the SRC is 1 A. At time 25 ms, the peak-to-peak of the SRC is 0.4 A. Compared to the control method C, the control method D not only makes the output voltages of parallel ESCs equivalent, eliminates the circulating current and improves the output current sharing between parallel ESCs, but also effectively reduces the SRC.

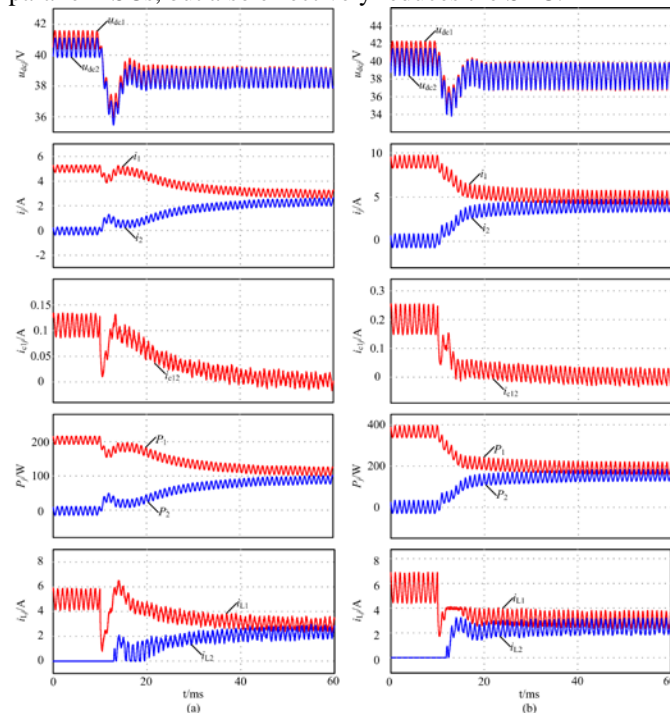


Fig. 18. Simulation results of the output voltage  $u_{dcj}$ , output current  $i_j$ , circulating current  $i_{c1j}$ , output power  $P_j$  and inductance current  $i_{Lj}$  under the different control method A and D with the number of AC loads. (a) single group AC loads with  $P_{o1}=200W$ . (b) two groups of AC loads with  $P_{o1}= P_{o2}= 200W$ .

With the number of single-phase AC loads increasing, the comparative simulation results of the output voltage  $u_{dcj}$ , output current  $i_j$ , circulating current  $i_{c1j}$ , output power  $P_j$  and inductance current  $i_{Lj}$  under the control method A and D are shown in Fig. 18. In Fig 18(a), single group AC loads is injected into DC MG, and its active power is approximately equal to 200W. The control method A is used to simulate for each ESC during time 0-10 ms, and the control method D is used to simulate for each ESC during time 10-60 ms. Initially, up to 10 ms, the output voltage of the 2<sup>nd</sup> ESC is decreased by 1% of its nominal value 41V, and the peak-to-peak of the SRC is 1 A. At time 40 ms, the output voltage of the 2<sup>nd</sup> ESC is equal to the output voltage of the 1<sup>st</sup> ESC and the peak-to-peak of the SRC is 0.4 A. Compared to the control method A, the control method D not only makes the output voltages of parallel ESCs equivalent, eliminates the circulating current and improves the output current sharing between parallel ESCs, but also effectively reduces the SRC.

In Fig 18(b), two groups of single-phase AC loads are injected into DC MG, where active power of each group AC loads is approximately equal to 200W. The procedure is the same as the one described above. Compared to the control method A, except the peak-to-peak of the SRC increasing continuously with increase in the number of single-phase AC loads, other conditions are equal to Fig. 18(a). Therefore, when the number of single-phase AC loads increases, the proposed control method is still applicable.

In order to verify the simulation results, the experimental platform of parallel ESCs in the low-voltage DC MG is built in Fig. 19, which is mainly composed of the batteries, ESCs, DC/AC inverters, LC filters and loads. The proposed control method is implemented by using TMS320F2812. Detailed system parameters are shown in Tab. III.

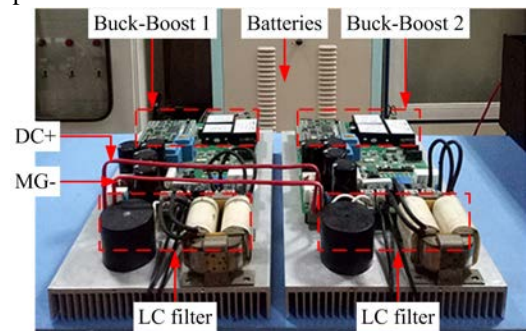


Fig. 19. Experimental platform of parallel ESCs.

The comparative experiments under different control methods including cases I, II, III and IV are shown in Fig. 20 and 21. Fig. 20 shows the experimental results of the ripple of DC bus voltage  $\Delta u_{dc}$ , ripple of the inductance current  $\Delta i_{L1}$  and output current of the inverter  $i_o$ . Seen from Fig. 20(a) and 20(b), the peak-to-peak of the SRC is 1 A in the case I and II, and the proportion is about 20.5%. But from Fig. 20(c) and 20(d), the peak-to-peak of the SRC is 0.3A in the case III and IV, which accounts for 6.15%. Therefore, the SRC in the inductance current is smaller in the case III and IV, which effectively reduce the SRC.

Fig. 21 shows the experimental results of the ripple of DC

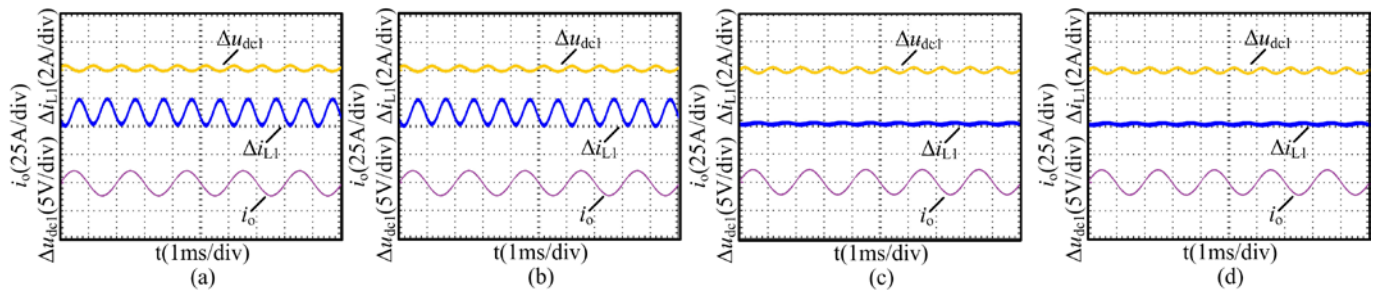


Fig. 20. Experimental results of the ripple of DC bus voltage  $\Delta u_{dc}$ , ripple of the inductance current  $\Delta i_{L1}$  and output current of the inverter  $i_o$  under different methods. (a) Case I. (b) Case II. (c) Case III. (d) Case IV.

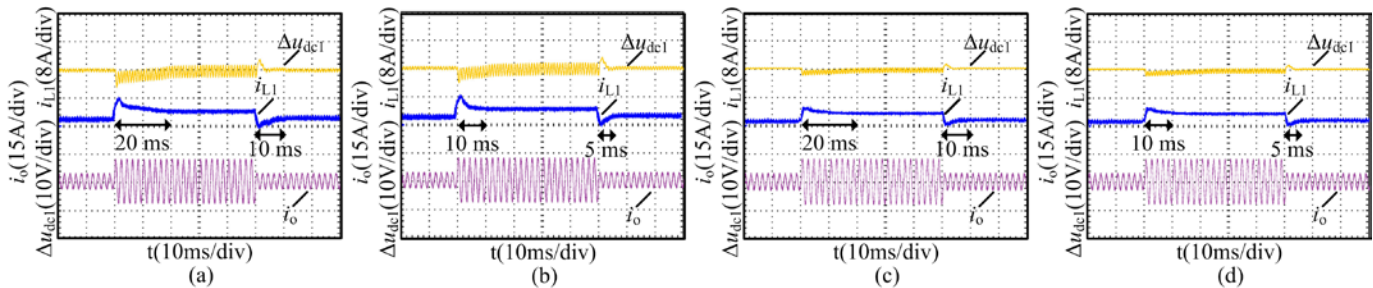


Fig. 21. Experimental results of the ripple of DC bus voltage  $\Delta u_{dc}$ , inductance current  $i_{L1}$  and output current of the inverter  $i_o$  with the loads suddenly changing under different methods. (a) Case I. (b) Case II. (c) Case III. (d) Case IV.

bus voltage  $\Delta u_{dc}$ , inductance current  $i_{L1}$  and output current of the inverter  $i_o$  when the loads suddenly increase from 33% to 100% or suddenly decrease from 100% to 33%. Seen from Fig. 21(a) and 21(c), the regulation time is 20 ms at the loads increased suddenly and the regulation time becomes 10 ms at the loads decreased abruptly in the case I and III. But from Fig. 21(b) and 21(d), the regulation time is 10 ms at the loads increasing suddenly, and the regulation time becomes 5 ms at the loads decreasing abruptly in the case II and IV, which improve the dynamic performance of the system at the load mutation. Therefore, the case IV not only effectively reduces the SRC, but also improves the dynamic performance of the system at the load mutation.

The single group of single-phase AC loads is injected into DC MG, and its active power is approximately equal to 200W. The experimental results of the output voltage  $u_{dcj}$  and circulating current  $i_{c1j}$  under different control methods with single group AC loads are shown in Fig. 22. From Fig. 22(a), during time 0-20 ms, the control method A is used to simulate for each ESC. During time 20-40 ms, the control method B is used to simulate for each ESC. Initially, up to 20 ms, the output voltage of the 2<sup>nd</sup> ESC is decreased by 1% of its nominal value 41V and the amplitude of the circulating current is about 1.2 A.

At time 30 ms, the deviation between the output voltage and the rated voltage for each ESC is 5% within the acceptable range, but the output voltages of parallel ESCs may have a certain deviation. And the amplitude of the circulating current is about 0.7 A. Compared to the control method A, the control method B reduces the output voltage deviation of parallel ESCs and suppresses the circulating current.

From Fig. 22(b), during time 0-20 ms, the control method B is used to simulate for each ESC. During time 20-40 ms, the control method C is used to simulate for each ESC. Initially, up to 20 ms, the deviation between the output voltage and the rated voltage for each ESC is 5% within the acceptable range, but the output voltages of parallel ESCs may have a certain deviation. And the amplitude of the circulating current is about 0.7 A. At time 30 ms, the output voltage of the 2<sup>nd</sup> ESC is equal to the output voltage of the 1<sup>st</sup> ESC and the amplitude of the circulating current is about 0.1 A. Compared to the control method B, the control method C makes the output voltages of parallel ESCs equivalent, eliminates the circulating current and improves the output current sharing between parallel ESCs.

From Fig. 22(c), during time 0-20 ms, the control method C is used to simulate for each ESC. During time 20-40 ms, the control method D is used to simulate for each ESC. The control

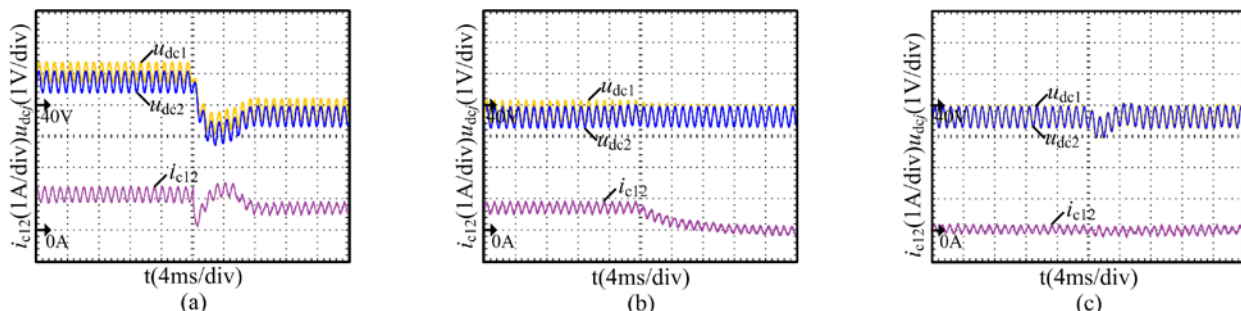


Fig. 22. Experimental results of the output voltage  $u_{dcj}$  and circulating current  $i_{c1j}$  under different control methods with single group AC loads. (a) the control method A and B. (b) the control method B and C. (c) the control method C and D.

method D has the advantages of the control method C. From Fig. 20 and Fig. 21, the SRC suppression method by two BPFs not only effectively reduces the SRC, but also improves the dynamic performance of the system at the load mutation. So, the control method D not only makes the output voltages of parallel ESCs equivalent, eliminates the circulating current and improves the output current sharing between parallel ESCs, but also effectively reduces the SRC.

With the number of single-phase AC loads increasing, the comparative experimental results of the output voltage  $u_{dcj}$  and circulating current  $i_{c1j}$  under the control method A and D are shown in Fig. 23. In Fig. 23(a), single group AC loads is injected into DC MG, and its active power is approximately equal to 200W. In Fig 23(b), two groups of single-phase AC loads are injected into DC MG, where active power of each group AC loads is approximately equal to 200W. The control method A is used to simulate for each ESC during time 0-10 ms, and the control method D is used to simulate for each ESC during time 10-60 ms. Obviously, with the number of the same AC loads increasing, initially, up to 10 ms, the output voltage of the 2<sup>nd</sup> ESC is decreased by 1% of its nominal value 41V and the amplitude of the circulating current is about 1.2 A in Fig. 23(a) and 2.2 A in Fig. 23(b). At time 40 ms, the output voltage of the 2<sup>nd</sup> ESC is equal to the output voltage of the 1<sup>st</sup> ESC in Fig. 23(a) and Fig. 23(b). Therefore, when the number of single-phase AC loads increases, the proposed control method is still applicable.

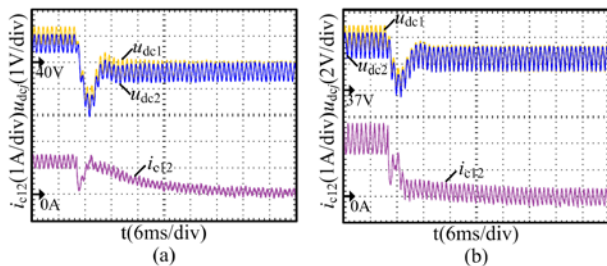


Fig. 23. Experimental results of the output voltage  $u_{dcj}$  and circulating current  $i_{c1j}$  under the control method A and D with the different number of AC loads. (a) single group AC loads. (b) two groups of AC loads.

## VI. CONCLUSION

In DC MG, when single-phase inverters with AC loads are injected to DC MG, instantaneous output power of single-phase inverters ripples at double output voltage frequency, which leads to generate the SRC. Meanwhile, the circulating current issue will arise if there is a mismatch in the output voltage deviation of parallel ESCs. In this paper, the SRC suppression by two BPFs and current sharing method is proposed, and conclusion is summarized as follow: The SRC suppression method by two BPFs for the ESC not only effectively reduces the SRC, but also improves the dynamic performance of the system at the load mutation. Thus the lifespan of the power converters are improved, and the current stress and conduction loss of the power switches are decreased. An adaptive droop control method by introducing the fine tuning virtual resistances is adopted to reduce the output voltage deviation of parallel ESCs and effectively suppress the circulating current.

## REFERENCES

- [1] T.-F. Wu, C.-L. Kuo, L.-C. Lin, and Y.-K. Chen, "DC-bus voltage regulation for a DC distribution system with a single-phase bidirectional inverter," *IEEE Journal of Emerging and Selected Topics in Power Electronics*, vol. 4, no. 1, pp. 210–220, Mar. 2016.
- [2] Y. Chen, J. M. Guerrero, Z. Shui, Z. Chen, L. Zhou, and A. Luo, "Fast reactive power sharing, circulating current and resonance suppression for parallel inverters using resistive-capacitive output impedance," *IEEE Trans. Power Electron.*, vol. 31, no. 8, pp. 5524–5537, Aug. 2016.
- [3] J. M. Guerrero, M. Chandorkar, T.-L. Lee, and P. C. Loh, "Advanced control architectures for intelligent microgrids-Part I: Decentralized and hierarchical control," *IEEE Trans. Ind. Electron.*, vol. 60, no. 4, pp. 1254–1262, Apr. 2013.
- [4] A. Darwish, D. Holliday, S. Ahmed, A. M. Massoud, and B. W. Williams, "A single-stage three-phase inverter based on cuk converters for PV applications," *IEEE Journal of Emerging and Selected Topics in Power Electronics*, vol. 2, no. 4, pp. 797–807, Dec. 2014.
- [5] P. Cairolì, I. Kondratiev, and R. A. Dougal, "Coordinated control of the bus tie switches and power supply converters for fault protection in DC microgrids," *IEEE Trans. Power Electron.*, vol. 28, no. 4, pp. 2037–2047, Apr. 2013.
- [6] Y.-K. Chen, Y.-C. Wu, C.-C. Song, and Y.-S. Chen, "Design and implementation of energy management system with fuzzy control for DC microgrid systems," *IEEE Trans. Power Electron.*, vol. 28, no. 4, pp. 1563–1570, Apr. 2013.
- [7] R. S. Balog, W. W. Weaver, and P. T. Krein, "The load as an energy asset in a distributed DC smartgrid architecture," *IEEE Trans. Smart Grid*, vol. 3, no. 1, pp. 253–260, Mar. 2012.
- [8] D. Dong, F. Luo, X. Zhang, D. Boroyevich, and P. Mattavelli, "Grid-interface bidirectional converter for residential DC distribution systems-Part 2: AC and DC interface design with passive components minimization," *IEEE Trans. Power Electron.*, vol. 28, no. 4, pp. 1667–1679, Apr. 2013.
- [9] J. He, Y. W. Li, and F. Blaabjerg, "Flexible microgrid power quality enhancement using adaptive hybrid voltage and current controller," *IEEE Trans. Ind. Electron.*, vol. 61, no. 6, pp. 2784–2794, Jun. 2014.
- [10] G. Fontes, C. Turpin, S. Astier, and T. A. Meynard, "Interactions between fuel cells and power converters: Influence of current harmonics on a fuel cell stack," *IEEE Trans. Power Electron.*, vol. 22, no. 2, pp. 670–678, Mar. 2007.
- [11] X. Li, W. Zhang, H. Li, R. Xie, M. Chen, G. Shen, and D. Xu, "Power management unit with its control for a three-phase fuel cell power system without large electrolytic capacitors," *IEEE Trans. Power Electron.*, vol. 26, no. 12, pp. 3766–3777, Dec. 2011.
- [12] Y. Gu, X. Xiang, W. Li, and X. He, "Mode-adaptive decentralized control for renewable DC microgrid with enhanced reliability and flexibility," *IEEE Trans. Power Electron.*, vol. 29, no. 9, pp. 5072–5080, Sep. 2014.
- [13] N. Femia, G. Petrone, G. Spagnuolo, and M. Vitelli, "A technique for improving P&O MPPT performance of dual-stage grid-connected photovoltaic systems," *IEEE Trans. Ind. Electron.*, vol. 56, no. 11, pp. 4473–4482, Nov. 2009.
- [14] S. K. Mazumder, R. K. Burra, and K. Acharya, "A ripple-mitigating and energy-efficient fuel cell power-conditioning system," *IEEE Trans. Power Electron.*, vol. 22, no. 4, pp. 1437–1452, Jul. 2007.
- [15] J.-M. Kwon, B.-H. Kwon, and K.-H. Nam, "Grid-connected photovoltaic multistring PCS with PV current variation reduction control," *IEEE Trans. Ind. Electron.*, vol. 56, no. 11, pp. 4381–4388, Nov. 2009.
- [16] W. Wang, and X. Ruan, "A modified reference of an intermediate bus capacitor voltage-based second-harmonic current reduction method for a standalone photovoltaic power system," *IEEE Trans. Power Electron.*, vol. 31, no. 8, pp. 5562–5573, Aug. 2016.
- [17] J. C. Rosas-Caro, F. Mancilla-David, J. C. Mayo-Maldonado, J. M. Gonzalez-Lopez, H. L. Torres-Espinosa, and J. E. Valdez-Resendiz, "A Transformer-less high-gain boost converter with input current ripple cancelation at a selectable duty cycle," *IEEE Trans. Ind. Electron.*, vol. 60, no. 10, pp. 4492–4499, Oct. 2013.
- [18] H.-L. Do, "Soft-switching SEPIC converter with ripple-free input current," *IEEE Trans. Power Electron.*, vol. 27, no. 6, pp. 2879–2887, Jun. 2012.
- [19] K.-C. Tseng, C.-C. Huang, and W.-Y. Shih, "A High step-up converter with a voltage multiplier module for a photovoltaic system," *IEEE Trans. Power Electron.*, vol. 28, no. 6, pp. 3047–3057, Jun. 2013.

- [20] C. Liu and J.-S. Lai, "Low frequency current ripple reduction technique with active control in a fuel cell power system with inverter load," *IEEE Trans. Power Electron.*, vol. 22, no. 4, pp. 1429–1436, Jul. 2007.
- [21] L. Zhang, X. Ren, X. Ruan, and Q. Chen, "Control strategy for the front-end DC-DC converter to reduce the second-order harmonic current in the two-stage inverter," in *Proc. IEEE APEC*, Mar. 2013, pp. 719–726.
- [22] R. Bojoi, C. Pica, D. Ruiu, and A. Tenconi, "New dc-dc converter with reduced low-frequency current ripple for fuel cell in single-phase distributed generation," in *Proc. IEEE Int. Conf. Ind. Technol.*, Mar. 2010, pp. 1213–1218.
- [23] S. Anand, and B. G. Fernandes, "Modified droop controller for paralleling of dc-dc converters in stand-alone dc system," *IET Power Electron.*, vol. 5, no. 6, pp. 782–789, Jul. 2012.
- [24] J. M. Guerrero, J. C. Vasquez, J. Matas, L. G. D. Vicuna, and M. Castilla, "Hierarchical control of droop-controlled ac and dc microgrids: A general approach toward standardization," *IEEE Trans. Ind. Electron.*, vol. 58, no. 1, pp. 158–172, Jan. 2011.
- [25] M. Hua, H. Hu, Y. Xing, and J. M. Guerrero, "Multilayer control for inverters in parallel operation without intercommunications," *IEEE Trans. Power Electron.*, vol. 27, no. 8, pp. 3651–3663, Aug. 2012.
- [26] X. Lu, J. M. Guerrero, K. Sun, and J. C. Vasquez, "An improved droop control method for dc microgrids based on low bandwidth communication with dc bus voltage restoration and enhanced current sharing accuracy," *IEEE Trans. Power Electron.*, vol. 29, no. 4, pp. 1800–1812, Apr. 2014.
- [27] H. Kakigano, Y. Miura, and T. Ise, "Distribution voltage control for DC microgrids using fuzzy control and gain-scheduling technique," *IEEE Trans. Power Electron.*, vol. 28, no. 5, pp. 2246–2258, May. 2013.
- [28] N. R. Chaudhuri, and B. Chaudhuri, "Adaptive droop control for effective power sharing in multi-terminal dc (MTDC) grids," *IEEE Trans. Power Syst.*, vol. 28, no. 1, pp. 21–29, Feb. 2013.
- [29] H.-H. Huang, C.-Y. Hsieh, J.-Y. Liao, and K.-H. Chen, "Adaptive droop resistance technique for adaptive voltage positioning in boost DC-DC converters," *IEEE Trans. Power Electron.*, vol. 26, no. 7, pp. 1920–1932, Jul. 2011.



**Ling Yang** (S'16) was born in Liaoning, China, 1992. She received the B.S. degree from the College of Electrical and Information Engineering, Hunan University, Changsha, China, in 2014. Currently, she has been working toward the Ph.D. degree in electrical engineering from Hunan University, Changsha, China.

Her research interests include power electronics, and distributed power systems.



**Yandong Chen** (S'13-M'14) was born in Hunan, China, in 1979. He received the B.S. and M.S. degree in instrument science and technology from Hunan University, Changsha, China, in 2003 and 2006, respectively, and the Ph.D. degree in electrical engineering from Hunan University, Changsha, China, in 2014. He has been an Associate Professor in the College of Electrical and Information Engineering, Hunan University, Changsha.

His research interests include power electronics for microgrid, distributed generation, power quality, and energy storage. Dr. Chen is a recipient of the 2014 National Technological Invention Awards of China, and the 2014 WIPO-SIPO Award for Chinese Outstanding Patented Invention. He is a member of IEEE Power Electronics Society.



**An Luo** (SM'09) was born in Changsha, China, in 1957. He received the B.S. and M.S. degrees in industrial automation from Hunan University, Changsha, in 1982 and 1986, respectively, and the Ph.D. degree in fluid power transmission and control from Zhejiang University, Hangzhou, China, in 1993. Between 1996 and 2002, he was a Professor with Central South University. Since 2003, he has been a Professor in the College of Electrical and Information Engineering, Hunan University, where he also serves as the Chief of National Electric Power Conversion and Control Engineering Technology Research Center.

His research interests mainly include distributed generation, microgrid, and power quality. He was elected to the Chinese National Academy of Engineering (CNAE) in 2015, the highest honor for scientists and engineers and scientists in China. He has won the highly prestigious China National Science and Technology Awards three times (2014, 2010 and 2006).



**Wenhua Wu** (S'16) was born in Hunan, China, 1991. He received the B.S. degree from the College of Electrical and Information Engineering, Hunan University, Changsha, China, in 2014. Currently, he has been working toward the Ph.D. degree in electrical engineering from Hunan University, Changsha, China.

His research interests include renewable energy generation systems, microgrid, power quality, and VSC-HVDC systems.



**Kunshan Huai** was born in Henan, China, 1991. He received the B.S. degree from the College of Electrical and Information Engineering, Hunan University, Changsha, China, in 2014. Currently, he has been working toward the professional degree in electrical engineering from Hunan University, Changsha, China.

His research interests include power electronics, and distributed power systems.



**Xiaoping Zhou** (S'16) was born in Jiangxi, China, 1990. He received the B.S. degree in electrical engineering from Hunan University, Changsha, China, in 2013. Currently, he has been working toward the Ph.D. degree in electrical engineering from Hunan University, Changsha, China.

His research interests include power electronics, distributed generation, microgrid, power quality and energy storage.



**Leming Zhou** was born in Hunan, China, in 1989. He received the B.S. and Ph.D. degree in electrical engineering from Hunan University, Changsha, China, in 2011 and 2016, respectively. Currently, he has been working postdoctoral research in electrical engineering from Hunan University, Changsha, China.

His research interests include power electronics for microgrid, distributed generation, and power quality.



**Qianming Xu** (S'15) was born in Henan, China, 1989. He received the B.S. degree in Electrical Engineering and Automation from the College of Electrical and Information Engineering, Hunan University, Changsha, China, in 2012. He has been working toward the Ph.D. degree in Electrical Engineering in the College of

Electrical and Information Engineering, Hunan University, Changsha since 2012.

His research interests include multilevel converters, power quality control, electric drive and power conversion control.



**Josep M. Guerrero** (S'01-M'04-SM'08-FM'15) received the B.S. degree in telecommunications engineering, the M.S. degree in electronics engineering, and the Ph.D. degree in power electronics from the Technical University of Catalonia, Barcelona, in 1997, 2000 and 2003, respectively. Since

2011, he has been a Full Professor with the Department of Energy Technology, Aalborg University, Denmark, where he is responsible for the Microgrid Research Program ([www.microgrids.et.aau.dk](http://www.microgrids.et.aau.dk)). From 2012 he is a guest Professor at the Chinese Academy of Science and the Nanjing University of Aeronautics and Astronautics; from 2014 he is chair Professor in Shandong University; from 2015 he is a distinguished guest Professor in Hunan University; and from 2016 he is a visiting professor fellow at Aston University, UK, and a guest Professor at the Nanjing University of Posts and Telecommunications.

His research interests is oriented to different microgrid aspects, including power electronics, distributed energy-storage systems, hierarchical and cooperative control, energy management systems, smart metering and the internet of things for AC/DC microgrid clusters and islanded minigrids; recently specially focused on maritime microgrids for electrical ships, vessels, ferries and seaports. Prof. Guerrero is an Associate Editor for the IEEE TRANSACTIONS ON POWER ELECTRONICS, the IEEE TRANSACTIONS ON INDUSTRIAL ELECTRONICS, and the IEEE Industrial Electronics Magazine, and an Editor for the IEEE TRANSACTIONS on SMART GRID and IEEE TRANSACTIONS on ENERGY CONVERSION. He has been Guest Editor of the IEEE TRANSACTIONS ON POWER ELECTRONICS Special Issues: Power Electronics for Wind

Energy Conversion and Power Electronics for Microgrids; the IEEE TRANSACTIONS ON INDUSTRIAL ELECTRONICS Special Sections: Uninterruptible Power Supplies systems, Renewable Energy Systems, Distributed Generation and Microgrids, and Industrial Applications and Implementation Issues of the Kalman Filter; the IEEE TRANSACTIONS on SMART GRID Special Issues: Smart DC Distribution Systems and Power Quality in Smart Grids; the IEEE TRANSACTIONS on ENERGY CONVERSION Special Issue on Energy Conversion in Next-generation Electric Ships. He was the chair of the Renewable Energy Systems Technical Committee of the IEEE Industrial Electronics Society. He received the best paper award of the IEEE Transactions on Energy Conversion for the period 2014-2015, and the best paper prize of IEEE-PES in 2015. In 2014, 2015, and 2016 he was awarded by Thomson Reuters as Highly Cited Researcher, and in 2015 he was elevated as IEEE Fellow for his contributions on “distributed power systems and microgrids.”